

Synthesis of Novel Electrospun Composite Nano Powders of the Quaternary Ti-Al-O-B System

Zohreh Ghadimi

Bu-Ali Sina University: Bu Ali Sina University

Hamid Esfahani (✉ h.esfahani@basu.ac.ir)

Bu-Ali Sina University: Bu Ali Sina University

Yousef Mazaheri

Bu-Ali Sina University: Bu Ali Sina University

Research Article

Keywords: Aluminum, Borides, Borates, Electrospinning, Nanoparticle, Titanium

Posted Date: September 1st, 2020

DOI: <https://doi.org/10.21203/rs.3.rs-68451/v1>

License:  This work is licensed under a Creative Commons Attribution 4.0 International License.

[Read Full License](#)

Synthesis of Novel Electrospun Composite Nano Powders of the Quaternary Ti-Al-O-B System

Zohreh Ghadimi, Hamid Esfahani^{1*}, Yousef Mazaheri

Department of Materials Engineering, Bu-Ali Sina University, Hamedan, Iran, P.O.B: 65178-38695

* Corresponding author: P.O.B: 65178-38695, Tel&Fax: +98-81-38381601-10, E-mail: h.esfahani@basu.ac.ir

Abstract

In the present work, electrospinning was applied to develop multicomponent oxide, boride, and borate nanostructures in a quaternary Ti-Al-O-B system. Different molar ratios of B/(Ti+Al) (0.8, 1.6, and 2.4) were employed and evaluated. Imaging with the field emission scanning electron microscope (FESEM) and the transmission electron microscope (TEM) revealed that after one hour of thermal treatment at 1100 °C, the hybrid electrospun nanofibers (NFs) in the fibrous platform transformed into nanoparticles (NPs), nano-needles, and nano-whiskers at B/(Ti+Al) molar ratios of 0.8, 1.6, and 2.4, respectively. The binding energies were investigated by X-ray photoelectron spectroscopy (XPS), whereas the phase study was conducted via the X-ray diffraction (XRD) technique. The results confirmed the formation of nanostructured ceramic powder platforms composed of the multiple components, namely oxides (e.g., B doped TiO₂; Al₂O₃), borides (TiB, TiB₂, Ti₂B₅, TiB₁₂, and AlB₂), and borates (TiBO₃; Al₁₈B₄O₃₃). Simultaneous thermal analysis (STA) of the Ti-Al-O-B mats indicated that the borides and borates formed consecutively at temperatures above 800 °C through reactions involving molten B₂O₃. We found that the obtained NPs were well arranged and sintered together throughout the fibers.

Keywords: Aluminum; Borides; Borates; Electrospinning; Nanoparticle; Titanium;

1. Introduction

Ceramic particles, due to having desirable physical, chemical, and mechanical properties, are widely used as catalysts, semiconductors, electromagnetics, filtration media, thermal insulators, fillers, and reinforcements [1-3]. Nanostructured ceramics such as nanoparticles (NPs) and nanofibers (NFs) have drawn much attention in particular applications due to their unique properties such as the high surface area to volume ratio, low density, low heat conductivity, high hardness and excellent toughness [4-5]. The development of multicomponent ceramic products from nanostructured oxides, borides, and borates is an efficient solution for overcoming the hardness, corrosion resistance, high melting point, and abrasive requirements of designed systems [7,8]. Thus, a quaternary Ti-Al-O-B system can logically be used for exhibiting outstanding oxides, borides, and borates of titanium and aluminum components on the nanoscale.

Titanium borides have stoichiometric diversity in the forms of TiB , TiB_2 , Ti_3B_4 , Ti_2B_5 as well as TiB_{12} [8,9]. Several routes, such as pack cementation, magnetron sputtering, and self-propagating high-temperature synthesis (SHS), have been developed to produce the titanium borides as well as titanium borate (TiBO_3) [10-12]. However, there is one main problem in the Ti-B system for production of some kinds of titanium borides. Some borides (e.g., Ti_2B_5 and TiB_{12}) are formed via particular production methods such as SHS [13]. Titanium boride powders have received considerable attention for mechanical applications due to the presence of covalent bonds within the titanium matrix [14,15]. The diffusion coefficient of B into the titanium matrix has a significant role in the formation of the specific kind of titanium boride [16]. According to the literature review, by controlling the production reactions in the solid-liquid $\text{TiO}_2\text{-B}_2\text{O}_3$ binary system, the desired titanium boride and borate species can be generated [17].

Aluminum borates ($\text{Al}_{18}\text{B}_4\text{O}_{33}$ and $\text{Al}_4\text{B}_2\text{O}_9$) are the main stable phases present in the $\text{Al}_2\text{O}_3\text{-B}_2\text{O}_3$ binary system. $\text{Al}_{18}\text{B}_4\text{O}_{33}$ is stable until up to 1900 °C and is generated with lower B_2O_3 amounts, whereas $\text{Al}_4\text{B}_2\text{O}_9$ is produced when more B_2O_3 is present and is stable only below 1100 °C [18]. Aluminum borates have a strong tendency toward taking a needle-like morphology [19]. Production of aluminum borate needles or whiskers occurs between 600 and 800 °C; these products are often utilized in metal alloys for reinforcement, insulation, and improving oxidation resistance [20,21]. It is noteworthy that their application is not limited to metal matrix; Wang et al. [22] utilized the one-dimensional $\text{Al}_{18}\text{B}_4\text{O}_{33}$ as a junction between

two alumina pieces at high temperatures. The AlB₂ powders can also be prepared via the aluminothermy reaction in the Al₂O₃-B₂O₃ binary system. This kind of boride can be used to induce oxidation resistance because it is decomposed into Al and B at high temperatures [23].

Several routes are available for the preparation of nanostructured ceramic NPs and NFs, including sol-gel, crystallization from molten salts, combustion synthesis, and melt spinning [24-26]. However, the electrospinning method presents a simple and cost-efficient process that yields continuous fibers with average diameters of nano to micrometers [27,28]. In fact, electrospinning has recently facilitated the synthesis of nanocomposite particles and nanostructured thin films [29,30]. There are two approaches toward developing ceramic NFs via the electrospinning procedure: ceramic reagents are either blended as ceramic NPs or dissolved into a polymer solution as ceramic precursors. It should be added that post-heat treatment may regulate the final product as amorphous to highly crystalized ceramic NFs [28]. Dai et al. [31] were the first to attempt the preparation of borate fibers; they simply synthesized the predominating Al₄B₂O₉ species and traces of Al₁₈B₄O₃₃ crystals via the electrospinning method. Later, Ozdemir et al. [32] investigated the role of the viscosity of the electrospinning solution for the production of aluminum borate NFs. In another experimentation with the electrospinning technique, Song et al. [33] studied the formation of mullite-type composite NFs in the Al₂O₃-SiO₂-B₂O₃ system. Nevertheless, there is a lack of studies regarding the NFs of borides and borates, especially in the ternary TiO₂-Al₂O₃-B₂O₃ system.

This study aimed to investigate the potential of the electrospinning procedure in the formation of diverse boride and borate nano-arrays of the quaternary Ti-Al-O-B system. The novelty of this study was the aim of achieving synergetic effects between titanium boride NPs and the aluminum borate nano-whiskers. Since the B/(Ti+Al) molar ratio has a significant impact on the physical and mechanical properties of borides [34], an electrospun Ti-Al-O-B powder was first synthesized using a B/(Ti+Al) molar ratio of 0.8. Afterward, Ti-Al-O-B powder samples were developed with two and three times higher boron contents (B/(Ti+Al) molar ratios of 1.6 and 2.4, respectively). Finally, a range of analytical experiments was conducted to facilitate an understanding of the mechanisms involved in the formation of the powders.

2. Materials and Methods

2.1. Fabrication of nanofibrous Ti-Al-O-B powders

The electrospinning method was applied to produce the fibrous Ti-Al-O-B mat. A hybrid electrospinning solution containing the polymer and ceramic reagents was prepared via a two-step process. First, appropriate amounts of aluminum nitrate ($\text{Al}(\text{NO}_3)_3 \cdot 9\text{H}_2\text{O}$, Merck-101063), boric acid (H_3BO_3 , Merck-100165), and TiO_2 NPs (PlasmaChem GmbH, P25) were dissolved in 3.5 ml of ethanol ($\text{C}_2\text{H}_5\text{OH}$, Merck-100983), with the B/(Ti+Al) molar ratio being set at 0.8. The solution was stirred for 2 h at room temperature followed by 45 min of ultra-sonication to obtain a homogenous solution. Secondly, the 0.6 g of polyvinylpyrrolidone (PVP, Merck 107443) was dissolved in the mentioned solution by 1 h of magnetic stirring and 45 min of ultra-sonication, which gave a clear solution. The hybrid solution was electrospun with high voltage direct current (25 kV). The distance between the aluminum foil and needle syringe was 15 cm, and the feeding rate was kept as 0.2 ml.h^{-1} . After drying at 80°C for 24 h, the achieved mat was peeled out for heat treatment at 1100°C for 1 h in air atmosphere. The heating rate was $4.5^\circ\text{C}\cdot\text{min}^{-1}$, and the cooling step was carried out slowly in the furnace. To understand the effects of boron content on the composition and morphology of the Ti-Al-O-B mat, the mentioned procedure was repeated with two and three times higher B/(Ti+Al) molar ratios. The B/(Ti+Al) molar ratio was changed from 0.8 up to 2.4 by adjusting the level of boric acid in solution. The composition of the electrospinning solution is given in Table 1, along with the sample codes.

2.2. Characterizations

The microstructures of the as-spun mats were studied by scanning electron microscopy (SEM, model JEOL JSM 840A). The powders were investigated using a field emission scanning electron microscope (FESEM; model T-Scan) equipped with an energy dispersive X-ray spectrometer (EDS). The ImageJ software (1.38x NIH USA) was applied to calculate the size of fibers and particle diameters. The binding energies of Ti, Al, O, and B were evaluated by X-ray photoelectron spectroscopy (XPS; model BESTEC) with monochromatic $\text{Al K}\alpha$ radiation ($h\nu=1486.7 \text{ eV}$). High-resolution scanning was performed with a binding energy of 1s for O and B, and 2p for Ti and Al. The XPS analysis was carried out under 10^{-10} mbar after sputtering with argon ions. The phase study of powders was conducted by X-ray diffraction technique (XRD; model Philips, PW1730 Xpert; 1° incidence angle; $k_\alpha \text{ Cu}$; $\lambda = 0.154 \text{ nm}$). The X'pert HighScore Plus software (Ver. 2.2b) was used to interpret the phase formation data. The thermal behavior of mats in the range of 25-1000 °C was studied by thermogravimetry (TG)

and differential thermal analysis (DTA) with a simultaneous thermal analyzer (STA; model PA Q600). The transmission electron microscope (TEM; model Philips EM208S, 100 kV) facilitated the high-resolution morphological characterization of the prepared ceramic particles.

3. Results

The synthesis of nanofibrous Ti-Al-O-B powders has not been reported before this study. Hence, to evaluate the balance of the precursors in the hybrid electrospun solution, the sample with a 0.8 molar ratio of B/(Ti+Al) was synthesized. The micrographs of the electrospun nanofibrous TAOB-0.8 mat before and after calcination are displayed in Fig. 1 (a and b). As seen, straight fibers without beads were formed via the electrospinning procedure. The average diameter of the hybrid fibers was 233 ± 16 nm, providing an appropriate platform for the synthesis of nanostructured ceramic Ti-Al-O-B products. The results showed that the hybrid straight fibers transformed into ceramic particles arranged into a fibrous structure. The average sizes of the particles and fibers were 94 ± 41 and 217 ± 39 nm, respectively. The findings confirmed that a nanostructured ceramic powder was synthesized via the electrospinning method.

To understand the intra-molecular bonds within the developed powder, XPS spectra were obtained concerning to the Ti, Al, O, and B elements. The spectra are shown in Fig. 2 confirm the presence of the Ti, Al, O, and B elements inside the ceramic powder. The Ti2p spectrum displays two main $2p_{3/2}$ and $2p_{1/2}$ peaks, corresponding with the Ti binding energy values of 458.4 and 464.2 eV, respectively. By de-convolution of the Ti2p spectra, it was found that the $2p_{3/2}$ and $2p_{1/2}$ peaks each consisted of three sub-peaks: Ti-O, Ti-O-B, and Ti-B. The results demonstrate that Ti was present in the ceramic Ti-Al-O-B powder sample in the forms of titanium oxide, titanium borate, and titanium boride [14]. The Al2p spectrum shows that the main peak centered at 74.4 eV is in actuality the sum of three peaks: a tiny Al-B peak, an intensive Al-O-B peak, and a relatively high Al-O bond [34]. According to the findings, it can be elucidated that Al probably was found in the ceramic Ti-Al-O-B mats as the aluminum oxide, aluminum boride, and aluminum borate phases. The O1s peak is difficult to interpret because oxides and borates have O1s peaks with overlapping binding energies [15]. The main O1s peak at 531.7 eV can be de-convoluted to three peaks concerning the O-Ti, O-Al, and O-B bonds [35]. According to the area under the peaks, it can be said that oxygen had similar direct bonds with the other elements inside the Ti-Al-O-B powder. The B1s spectrum revealed

a high peak at 192.8 eV related to B in the B_2O_3 compound, a medium peak at 190.9 eV related to B in aluminum borate [7], and a small peak at 187.3 eV related to B in titanium borides [14]. Finally, we did not find a peak relevant to the Ti-Al binding energy, meaning that Ti and Al individually formed the ternary Ti-O-B and Al-O-B compounds inside the ceramic Ti-Al-O-B powder samples.

The binding energy spectra indicated that the oxides, borides, and borates of titanium and aluminum were candidates for the phasic composition of the nanofibrous Ti-Al-O-B powder sample. The XRD pattern of the synthesized nanofibrous TAOB-0.8 shown in Fig. 3 (a) enabled the interpretation of the composition of the Ti-Al-O-B powder. The highly peaked pattern demonstrates a complex and poly-crystallized composition for this platform. By pattern identification, it was found that the titanium had three different phases: titanium oxide, titanium borides, and titanium borate. The anatase- TiO_2 (as a precursor) became exchanged with the B doped rutile- TiO_2 ($TiB_{0.024}O_2$) in accordance with the 01-087-0921 JCPDS card. Diverse titanium borides, including TiB , TiB_2 , and Ti_2B_5 , were identified considering the (01-089-3922), (01-075-1045), and (00-006-0528) standard JCPDS cards. Significant peaks were attributed to the $TiBO_3$ (00-017-0310) phase. The results also confirmed that the aluminum became crystallized in the form of Al_2O_3 (JCPDS card 00-048-0366), AlB_2 (JCPDS card 00-039-1483), and $Al_{18}B_4O_{33}$ (JCPDS card 00-032-0003) phases after calcination of the electrospun Ti-Al-O-B mat at 1100 °C. Therefore, it can be said that the composition of the Ti-Al-O-B powder consisted of oxides (e.g., B doped TiO_2 and Al_2O_3), borides (TiB , TiB_2 , Ti_2B_5 , and AlB_2), and borates ($TiBO_3$ and $Al_{18}B_4O_{33}$). Higher B/(Ti+Al) molar ratios (1.6 and 2.4) were applied to understand the effects of the amount of B in the hybrid electrospun Ti-Al-O-B mat on the composition and morphology of the Ti-Al-O-B powder sample. The XRD patterns of the mentioned mats are presented in Fig. 3 (b and c). The results show that with increasing the B amount, the composition remained the same as the one described in the TAOB-0.8 powder. However, the amount of B doped TiO_2 and Al_2O_3 decreased, while the amounts of AlB_2 and $Al_{18}B_4O_{33}$ increased. Furthermore, TiB_{12} (JCPDS card; 00-052-0843) was added to the Ti-Al-O-B powder sample when the B/(Ti+Al) molar ratio was adjusted to 2.4. Our findings demonstrate that no metallic phase corresponding to biphasic Al-Ti was formed in each sample when changing the B/(Ti+Al) molar ratio.

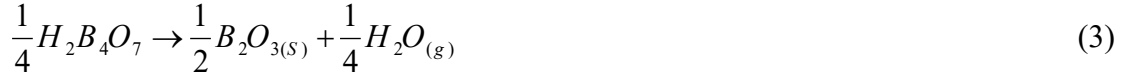
For morphological comparison of the Ti-Al-O-B powders, the FESEM images shown in Fig. 4 (a to c) were examined. As seen, sintered particles with an average size of 94 nm were present besides larger particles (up to 275 nm) in the TAOB-0.8 powder; most particles had polygonal

and sphere-like morphology. In contrast, finer particles with needle-like morphology were observed for the powders in the TAOB-1.6 powder. In addition, the larger particles vanished, though some spherical particles remained inside the powder. According to the micrograph illustrated in Fig. 4 (b), needle-like particles with an average width of 44 ± 5 nm and an average length of 113 ± 19 nm were the major component of the TAOB-1.6 powder. By enhancing the B/(Ti+Al) molar ratio up to 2.4, whisker-shaped powders with an average width of 62 ± 18 nm and an average length of 595 ± 186 nm replaced the needle-like powders; few spherical particles were also observed.

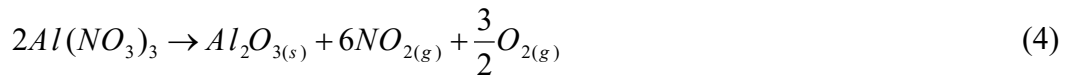
The surface EDS spectra of all Ti-Al-O-B powders are provided as graphs in Fig. 5 (a to c). The results confirm that Ti, Al, O, and B were the main elements of all powders. The absence of a C peak indicates that the PVP polymers present in the hybrid fibers were completely eliminated over calcination of the electrospun Ti-Al-O-B mat at 1100 °C. Furthermore, the B/(Ti+Al) molar ratios were calculated based on the atomic percent obtained via the EDS spectra. It was found that the calculated B/(Ti+Al) molar ratios were 0.69, 1.53, and 2.95 in the TABO-0.8, TABO-1.6, and TABO-2.4 powders, respectively, demonstrating good estimations.

4. Discussion

The XPS and XRD analyses indicated that no phase corresponding to the Al-Ti, Al-Ti-O, or Al-Ti-B systems had formed. Therefore, the possible growth mechanism of the Ti-Al-O-B powder from a hybrid electrospun polymer/ceramic mat should be described based on the thermal behaviors and individual chemical reactions between the $\text{TiO}_2\text{-B}_2\text{O}_3$ and $\text{Al}_2\text{O}_3\text{-B}_2\text{O}_3$ oxide systems [36]. Fig. 6 (a) presents a schematic cross-sectional view of a hybrid polymer/ceramic fiber, including an amorphous Al-O-B and TiO_2 NPs dissolved in the PVP matrix. The STA curves (including TG and DTA) of all mats are presented in Fig. 7 (a and b). The results show that weight loss commenced immediately at the beginning of the process. The endothermic peaks below 200 °C are attributed to the loss of structural water from boric acid and formation of the $\text{H}_2\text{B}_4\text{O}_7$ compound through Eqs. 1 and 2, respectively. The decomposition of boric acid to B_2O_3 was completed at 250 °C (Eq. 3) [18]. The solid B_2O_3 particles can distribute homogeneously within a fiber due to the homogenous nature of the electrospinning solution. During the exit of H_2O vapor, micro-cracks are generated alongside the PVP matrix, facilitating PVP decomposition. Fig. 6 (b) shows the schematic processes of solid B_2O_3 formation and cracking by H_2O vapor.



The results of the STA analysis depicted in Fig. 7 (a and b) confirm the decomposition of $Al(NO_3)_3$ at 350-400 °C, which is one of the vital reactions that occurred in the Ti-Al-O-B system. This is because Al_2O_3 sites are potential nuclei for the formation of aluminum boride and aluminum borate within the fibers. The schematic presentation of this phenomenon is presented in Fig. 6 (c). The decomposition of $Al(NO_3)_3$ took place with a weight loss of 20-30 % in all samples due to the remarkable production of the NO_2 and O_2 off-gases based on Eq. 4 [37].

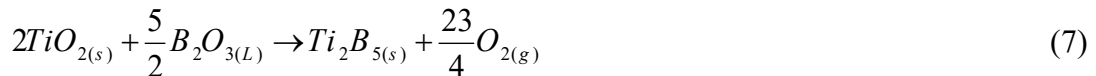


With further increase in temperature, the homogenously dispersed solid B_2O_3 became smelted at 450 °C, before the molten B_2O_3 surrounded the Al_2O_3 nuclei as well as the TiO_2 NPs inside the fibers (Fig. 6 (d)). According to the STA analysis, with a further increase in temperature, the decomposition of PVP was intensified (Fig. 7). The PVP matrix was wholly eliminated at 600-650 °C, and the initial weight of the platforms declined by approximately 78, 82, and 86 % with respect to the TAOB-0.8, TAOB-1.6, and TAOB-2.4 samples, respectively. After the PVP matrix weight residue became zero, a ceramic matrix containing solids and liquids remained throughout the fibers, as schematically presented in Fig. 6 (e). The number and nature of the solids have significant roles in solid-liquid reactions [38]. The EDS spectra confirmed the absence of the C element inside all powders. Above 800 °C, the circumstances for the production of borides and borates are provided via the vapor-liquid-solid reactions as not only solids were covered by the molten B_2O_3 , but also a matrix based on the molten B_2O_3 was formed [39]. The DTA curves in the range of 800 to 1000 °C shown in Fig. 7 (c) allowed the identification of peaks corresponding with borides and borates. Further studies were performed by the derivative of heat to temperature ($dH.dT^{-1}$) in the range of 800 to 1000 °C to understand the formation of the borides and borates. Figure 7 (d) presents the complex temperatures for assuming the formation of the boride and borate species. According to the studies, the number of exothermic peaks increased, and the heat flow intensified after increasing the B/(Ti+Al)

molar ratio. In other words, a higher amount of B_2O_3 relative to Al and Ti oxides promotes the formation of borides and borates. The unreacted TiO_2 NPs reacted specifically with the surrounding molten B_2O_3 , and thus TiB was generated according to Eq. 5.



The O_2 gas penetrates the TiO_2 NPs and causes particle breakage. The broken TiO_2 NPs, having a higher surface area, react more readily with B_2O_3 . The mechanism of TiO_2 NP breakage is presented in Fig.6 (f), along with the mechanism of the formation of titanium boride grains inside a fiber. With higher molten B_2O_3 presence, other titanium borides such as TiB_2 and Ti_2B_5 are formed (see Eqs. 6 and 7). Following the findings of Lepakova et al. [8], it should be added that light layers of Ti_2B_5 can appear around the previously-formed TiB_2 grains. The XRD analysis indicated that an extra titanium boride (TiB_{12}) was also generated inside the TAOB-2.4 powder. Based on reaction 8, this titanium boride, which is highly rich in boron, was formed by the B_2O_3 compound at a higher stoichiometric ratio.

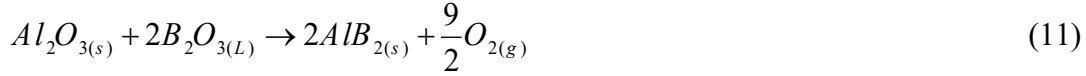


The vast amount of hot O_2 gas caused the oxidation of TiB to $TiBO_3$ shown in Eq. 9 [40]. The presence of titanium borate within all the powders was confirmed by both the XRD and the $2p_{3/2}$ and $2p_{1/2}$ peaks present in the XPS spectrum of Ti. The re-consumption of TiB in the oxidation reaction was the main reason for its low amount in the final products.

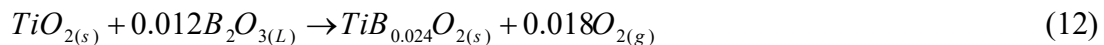


Notably, the reactions between the Al_2O_3 nuclei and molten B_2O_3 also took place at above 800 °C [22,32]. The majority of the Al_2O_3 crystals were replaced with $Al_{18}B_4O_{33}$ according to Eq. 10, and homogenously dispersed $Al_{18}B_4O_{33}$ grains were therefore created alongside the fibers (see Fig. 6 (f)). The AlB_2 phase also can be synthesized directly via the reaction between Al_2O_3 nuclei and molten B_2O_3 at elevated temperature, as shown in Eq. 11, respectively [23]. The XRD patterns revealed that the amount of AlB_2 was low in comparison with $Al_{18}B_4O_{33}$. This is

because most of the $\text{Al}(\text{NO}_3)_3$ transformed into the Al_2O_3 nuclei, and $\text{Al}_{18}\text{B}_4\text{O}_3$ subsequently replaced the Al_2O_3 nuclei.



With increased temperature and the presence of more B_2O_3 within the powders, all titanium and aluminum borate and boride particles grew in size. As schematically presented in Fig. 6 (g), grain growth continued until the grains could attach well together. Intra-grain diffusion was activated at the flat grain boundaries [41], and the grown grains consequently became sintered together well by a shrinkage throughout the fiber diameter, as shown in Fig. 6 (h) [42]. The sintering of borides, borates, and oxides together created the brittle fibers that may break to shorter fragments. The microscopic findings obtained from Fig. 4 (a) obviously confirm the fibrous microstructure constructed by the sintering of NPs. It is worth mentioning that although the borides have difficult sintering behavior due to the presence of strong covalent bonds [43], the nanostructured platform promoted sintering because of the high surface area to volume and the large number of particle junctions. Our findings also demonstrate that with augmentation of the $\text{B}/(\text{Ti}+\text{Al})$ molar ratio to 1.6, nano needle-like particles became the primary constructive agents of the powder. Grain growth in a preferred crystallography orientation is a significant specification of $\text{Al}_{18}\text{B}_4\text{O}_{33}$ [44]. The reaction between Al_2O_3 nuclei and molten B_2O_3 (Eq. 10) intensified when the $\text{B}/(\text{Ti}+\text{Al})$ molar ratio was increased up to 2.4. In subsequence, the needle-like grain growth of $\text{Al}_{18}\text{B}_4\text{O}_{33}$ also intensified, leading to the formation of $\text{Al}_{18}\text{B}_4\text{O}_{33}$ whiskers, as confirmed by the micrographs shown in Fig. 4 (c). It is worth mentioning that not only $\text{Al}_{18}\text{B}_4\text{O}_{33}$ but also titanium borides and aluminum boride might be formed as columnar grains texture [17,45]. Furthermore, un-reacted Al_2O_3 nuclei may remain as the oxide phase inside the powders since the XRD patterns confirmed that the amount of aluminum oxide decreased with increased $\text{B}/(\text{Ti}+\text{Al})$ molar ratios. Phase identification in XRD analysis showed that the un-reacted TiO_2 NPs probably were doped by boron atoms at elevated temperatures. This phenomenon can be interpreted by Eq. 12 [46]. The unbroken TiO_2 NPs might have remained as spherical particles inside the powders. The TEM images of the Ti-Al-O-B powders obtained from different $\text{B}/(\text{Ti}+\text{Al})$ molar ratios (Fig. 8) are in good agreement with our findings, confirming the mentioned mechanism.



4. Conclusions

Nanostructured Ti-Al-O-B powders were synthesized via the electrospinning method with different B/(Ti+Al) molar ratios of 0.8, 1.6, and 2.4. The binding energy analysis by XPS technique and phase studies by XRD analysis showed that multiple components of oxides (e.g., B doped TiO_2 ; Al_2O_3), borides (TiB , TiB_2 , Ti_2B_5 , TiB_{12} , and AlB_2) and borates (TiBO_3 ; $\text{Al}_{18}\text{B}_4\text{O}_{33}$) formed the nanostructured ceramic powders. With increased B/(Ti+Al) molar ratios, the amounts of Al_2O_3 and TiO_2 decreased, whereas the amount of $\text{Al}_{18}\text{B}_4\text{O}_{33}$ increased. The FESEM and TEM micrographs also demonstrated that the polygonal NPs (94 ± 41 nm) were replaced with needle-like NPs (44 ± 5 nm wide, and 113 ± 19 nm length) and nano-whiskers (62 ± 18 nm wide, and 595 ± 186 nm length) when adjusting the B/(Ti+Al) molar ratio to 1.6 and 2.4, respectively. The thermal behavior of electrospun Ti-Al-O-B mats indicated that the borides and borates consecutively formed by reaction with molten B_2O_3 . It was found that the exit of hot gases had a significant role in the rearrangement of materials throughout the fibers. The electrospinning procedure provided an appropriate condition for the sintering of ceramic nano-arrays. Eventually, it can be concluded that electrospinning is a promising method for the fabrication of multicomponent oxide, boride, and borate nanostructures for various applications.

References

- [1]. Y. Xin, Y. Takeuchi, M. Hattori, T. Shirai, Enhanced electrical conductivity of alumina/nano-carbon ceramic composite via iodine impregnation of gel-casted alumina body and reductive sintering, *J. Eur. Ceram. Soc.*, 39 (14) (2019) 4440-4444. <https://doi.org/10.1016/j.jeurceramsoc.2019.06.002>.
- [2]. Y. Mazaheri, M. Meratian, R. Emadi, A. R. Najarian, Comparison of microstructural and mechanical properties of Al–TiC, Al–B₄C and Al–TiC–B₄C composites prepared by casting techniques, *Mat. Sci. Eng. A-Struct.*, 560 (2013) 278-287. <https://doi.org/10.1016/j.msea.2012.09.068>.
- [3]. Z. Yu, Y. Yang, K. Mao, Y. Feng, O. Wen, R. Riedel, Single-source-precursor synthesis and phase evolution of SiC-TaC-C ceramic nanocomposites containing core-shell structured TaC@C nanoparticles. *J. Adv. Ceram.*, 9, (2020) 320–328. <https://doi.org/10.1007/s40145-020-0371-z>
- [4]. M. Rostampour, S. Eavani, Synthesis and characterization of the novel nano composite pigments using CoWO₄ on different silica sources: A comparative study, *Powder Technol.*, 363, (2020) 86-94. <https://doi.org/10.1016/j.powtec.2020.01.031>.
- [5]. J. Du, A.P. Sanders, V. Jindal, K.S. Ravi Chandran, Rapid in situ formation and densification of titanium boride (TiB) nano-ceramic via transient liquid phase in electric field activated sintering, *Scripta Mater.*, 123 (2016) 95-99. <https://doi.org/10.1016/j.scriptamat.2016.06.010>.
- [6]. E. Salahi, H. Esfahani, I. Mobasherpour, M.A. Bijarchi, M. Taheri, Sintering behavior and mechanical properties of alumina/zirconia multilayers composite via nano-powder processing, *Ceram. Int.*, 40 (2014) 2717–2722. <https://doi.org/10.1016/j.ceramint.2013.10.051>.
- [7]. H. S. Song, J. Zhang, J. Lin, S. J. Liu, J. J. Luo, Y. Huang, E. M. Elssfah, A. Elsanousi, X. X. Ding, J. M. Gao, and Chengcun Tang, Coating Aluminum Borate (Al₁₈B₄O₃₃) Nanowire Webs with BN, *J. Phys. Chem. C*, 111 (2007) 1136-1139. <https://doi.org/10.1021/jp067393u>
- [8]. O. K. Lepakova, L. G. Raskolenko, and Yu. M. Maksimov, Titanium Borides Prepared by Self-Propagating High-Temperature Synthesis, *J. Inorg. Mater.*, 36 (6), (2000), 568-575. Doi: 1685/00/3606-0568525.00.
- [9]. B. Sarma, N.M.Tikekar, K.S.Ravi Chandran, Kinetics of growth of superhard boride layers during solid state diffusion of boron into titanium, *Ceram. Int.*, 38 (2012) 6795–6805. <https://doi.org/10.1016/j.ceramint.2012.05.077>.
- [10]. T. Moscicki, R. Psiuk, H. Słomińska, N. Leviant-Zayonts, D. Garbiec, M. Pisarek, P. Bazarnik, S. Nosewicz, J. Chrzanowska-Giżyńsk, Influence of overstoichiometric boron and titanium addition on the properties of RF magnetron sputtered tungsten borides, *Surf. Coat. Tech.*, 390 (2020) 125689. <https://doi.org/10.1016/j.surfcoat.2020.125689>.
- [11]. S.K. Mishra, V. Gokul, S.Paswan, Alumina-titanium diboride in situ composite by self-propagating high-temperature synthesis (SHS) dynamic compaction: Effect of compaction

pressure during synthesis, Int. J. Refract. Met. H., 43 (2014) 19-24. <https://doi.org/10.1016/j.ijrmhm.2013.10.018>.

[12]. A. Ebrahimi, H. Esfahani, A. Fattah-alhosseini, O. Imantalab, In-vitro electrochemical study of TiB/TiB₂ composite coating on titanium in Ringer's solution, J. Alloy. Compd., 765 (2018) 826-834. <https://doi.org/10.1016/j.jallcom.2018.06.312>.

[13]. M. Masanta, S.M. Shariff, A. Roy Choudhury, Microstructure and properties of TiB₂-TiC-Al₂O₃ coating prepared by laser assisted SHS and subsequent cladding with micro-/nano-TiO₂ as precursor constituent, Mater. Design, 90 (2016) 307-317. <https://doi.org/10.1016/j.matdes.2015.10.135>.

[14]. J. Liu, B. Blanpain, P. Wollants, A XPS Study of Atmospheric Plasma Sprayed TiB₂ Coatings, Key Engineering Materials, 368-372, (2008), 1347-1350. doi:10.4028/www.scientific.net/KEM.368-372.1347.

[15]. J. Cheng Ding, T. Fei Zhang, J. Moon Yun, K. Ho Kim, Q. Min Wang, Effect of Cu addition on the microstructure and properties of TiB₂ films deposited by a hybrid system combining high power impulse magnetron sputtering and pulsed dc magnetron sputtering, Surf. Coat. Tech., 344 (2018) 441–448. <https://doi.org/10.1016/j.surfcoat.2018.03.026>.

[16]. K. Morsi, V. V. Patel, Processing and properties of titanium–titanium boride (TiB_w) matrix composites—a review, J. Mater. Sci., 42 (2007) 2037–2047. <https://doi.org/10.1007/s10853-006-0776-2>.

[17]. Z. Jiang, W. E. Rhine, Preparation of Titanium Diboride from the Borothermic Reduction of TiO₂, TiOx(OH)y, Ti(O-n-Bu)₄-Derived Polymers, J. Eur. Ceram. Soc., 12 (1993) 403-411. [https://doi.org/10.1016/0955-2219\(93\)90011-F](https://doi.org/10.1016/0955-2219(93)90011-F).

[18]. M. F. Hernández, G. Suárez, M. Cipollone, M. S. Conconi, E. F. Aglietti, N. M. Rendtorff, Formation, microstructure and properties of aluminum borate ceramics obtained from alumina and boric acid, Ceram. Int., 43 (2) (2017) 2188-2195. <https://doi.org/10.1016/j.ceramint.2016.11.002>.

[19]. Z. Yu, N. Zhao, E. Liu, Ch. Shi, X. Du, J. Wang, Low-temperature synthesis of aluminum borate nanowhiskers on the surface of aluminum powder promoted by ball-milling pretreatment, Powder Technol., 212 (2) (2011) 310-315. <https://doi.org/10.1016/j.powtec.2011.06.003>

[20]. H. Esfahani, A. Abdollahzadeh, F. Dabir, Mahsa Rasouli Samar, Enhanced surface protection of in-738lc ni based alloy by metallic borides and aluminium borate coating via short time powder pack method, Article in Press, Protection of Metals and Physical Chemistry Of Surfaces, 56(3) (2020) 567-574. [Hhttps://doi:10.1134/S2070205120030144](https://doi.org/10.1134/S2070205120030144).

[21]. H.Y. Yue, B. Wang, X. Gao, S.L. Zhang, X.Y. Lin, L.H. Yao, E.J. Guo, Effect of interfacial modifying on the microstructures, mechanical properties and abrasive wear properties of aluminum borate whiskers reinforced 6061Al composite, J. Alloy. Compd., 692 (2017) 395-402. <https://doi.org/10.1016/j.jallcom.2016.09.082>.

- [22]. Y. Wang, J. Feng, Z. Wang, X. Song, J. Cao, Joining of Al₂O₃ by epitaxial growth of aluminum borate whiskers for high-temperature applications, *Mater. Lett.*, 163 (2016) 231–235. <https://doi.org/10.1016/j.matlet.2015.10.079>.
- [23]. D. Guo, Y. Zhao, C. Ling, J. Li, H. Jin, Vacuum freeze-drying assisted preparation of spherical AlB₂ powders with ultrafine microstructure, *Ceram. Int.*, 44(6) (2018) 6451-6455. <https://doi.org/10.1016/j.ceramint.2018.01.040>.
- [24]. S. Tautkus, K. Ishikawa, R. Ramanauskas, A. Kareiva, Zinc and chromium co-doped calcium hydroxyapatite: Sol-gel synthesis, characterization, behaviour in simulated body fluid and phase transformations, *J. Solid. State. Chem.*, 284 (2020) 121202. <https://doi.org/10.1016/j.jssc.2020.121202>.
- [25]. H. Wu, W. Pan, D. Lin, Electrospinning of ceramic nanofibers: Fabrication, assembly and applications. *J. Adv. Ceram.*, 1, (2012) 2–23. <https://doi.org/10.1007/s40145-012-0002-4>.
- [26]. A. A. Altaf, M. Ahmed, M. Hamayun, S. Kausar, M. Waqar, A. Badshah, Titania nanofibers: A review on synthesis and utilities, *Inorg. Chim. Acta.*, 501 (2020) 119268. <https://doi.org/10.1016/j.ica.2019.119268>.
- [27]. M.V. Someswararao, D. Pradeep, R.S. Dubey, P.S.V. Subbarao, Experimental Investigation of Electrospun Titania Nanofibers: An Applied Voltage Influence, *Mater. Today: Proceedings*, 18 (2019) 384–388. <https://doi.org/10.1016/j.matpr.2019.06.315>.
- [28]. H. Esfahani, R. Jose, S. Ramakrishna, Electrosprun Ceramic Nanofiber Mats Today: Synthesis, Properties, and Applications, *Materials*, 10(11), (2017), 1238. <http://doi:10.3390/ma10111238>.
- [29]. S. Osali, H. Esfahani, F. Dabir, P. Tajaslan, Structural and electro-optical properties of electrospun Cu-Doped ZnO thin films, *Solid. State. Sci.*, 98, (2019), 106038. <https://doi.org/10.1016/j.solidstatesciences.2019.106038>.
- [30]. M.P. Prabhakaran, M. Zamani, B. Felice, S. Ramakrishna, Electrospraying technique for the fabrication of metronidazole contained PLGA particles and their release profile, *Mat. Sci. Eng. C-Mater.*, 56(1) (2015) 66-73. <https://doi.org/10.1016/j.msec.2015.06.018>.
- [31]. H. Dai, J. Gong, H. Kim, D. Lee, A novel method for preparing ultra-fine alumina-borate oxide fibres via an electrospinning technique, *Nanotechnology*, 13 (2002) 674–677. <https://doi.org/10.1088/0957-4484/13/5/327>.
- [32]. M. Ozdemir, E. Celik, U. Cocen, Effect of viscosity on the production of alumina borate nanofibers via electrospinning, *Mater. Technol.*, 47 (2013) 735–738.
- [33]. X. Song, W. Liu, S. Xu, J. Wang, B. Liu, Q. Cai, S. Tang, Y. Ma, Microstructure and elastic modulus of electrospun Al₂O₃-SiO₂-B₂O₃ composite nanofibers with mullite-type structure prepared at elevated temperatures, *J. Eur. Ceram. Soc.*, 38 (1) (2018) 201-210. <https://doi.org/10.1016/j.jeurceramsoc.2017.08.007>.
- [34]. N. Nedfors, S. Mráz, J. Palisaitis, P. O.Å. Persson, H. Lind, S. Kolozsvari, J. M. Schneider, J. Rosen, Influence of the Al concentration in Ti-Al-B coatings on microstructure

and mechanical properties using combinatorial sputtering from a segmented TiB₂/AlB₂ target, *Surf. Coat. Tech.*, 364 (2019) 89–98. <https://doi.org/10.1016/j.surfcoat.2019.02.060>.

[35]. J. Yuan, Z. Zhang, M. Yang, F. Guo, X. Men, W. Liu, TiB₂ reinforced hybrid-fabric composites with enhanced thermal and mechanical properties for high-temperature tribological applications, *Tribol. Int.*, 115 (2017) 8–17. <https://doi.org/10.1016/j.triboint.2017.05.006>.

[36]. S.A.M. Chichi, M. N. Hamidon, M. Ertugrul, M. S. Mamat, H. Jaafar, N. Aris, Influence of B₂O₃ Addition on the Properties of TiO₂ Thick Film at Various Annealing Temperatures for Hydrogen Sensing. *Journal of Elec Mater*, 49 (2020) 3340–3349. <https://doi.org/10.1007/s11664-020-08059-0>.

[37]. J. Wang, L. Sha, Q. Yang, Y. Wang, D. Yang, Synthesis of aluminium borate nanowires by sol–gel method, *Mater. Res. Bull.*, 40 (2005) 1551–1557. <https://doi.org/10.1016/j.materresbull.2005.04.016>

[38]. V. Raghavan, Al-B-Ti (Aluminum-Boron-Titanium), *J. Phase Equilib. Diff.*, 26(2) (2005) 173–174. <http://DOI:10.1361/15477030523058>.

[39]. X.F. Duan, J.F. Wang, C.M. Lieber, Synthesis and optical properties of gallium arsenide nanowires *Appl. Phys. Lett.* 76 (2000) 1116. <https://doi.org/10.1063/1.125956>.

[40]. E. Zhang, G. Zeng, S. Zeng, Oxidation behavior of in situ TiB short fibre reinforced Ti-6Al-1.2B alloy in air. *J. Mater. Sci.*, 37 (2002) 4063–4071. <https://doi.org/10.1023/A:1020019431992>.

[41]. J. Zhang, F. Meng, R. I. Todd, Z. Fu, The nature of grain boundaries in alumina fabricated by fast sintering, *Scripta Mater.*, 62(9) (2010) 658–661. <https://doi.org/10.1016/j.scriptamat.2010.01.019>.

[42]. T.S. Srivatsan, G. Guruprasad, D. Black, R. Radhakrishnan, T.S. Sudarshan, Influence of TiB₂ content on microstructure and hardness of TiB₂–B₄C composite, *Powder Technol.*, 159 (3) (2005) 161–167. <https://doi.org/10.1016/j.powtec.2005.08.003>.

[43]. G.V. Samsonov, B.A. Kovenskaya, II. The Nature of the Chemical Bond in Borides. In: Matkovich V.I. (eds) *Boron and Refractory Borides*. Springer, Berlin, Heidelberg, 1977.

[44]. S. C. Xu, L.D. Wang, P.T. Zhao, W. L. Li, Z. W. Xue, W. D. Fei, Fiber texture evolution of hot-rolled aluminum matrix composite reinforced by aluminum borate whisker, *Mat. Sci. Eng. A-Struct.*, 533 (2012) 82–86. <https://doi.org/10.1016/j.msea.2011.11.038>.

[45]. P.H. Mayrhofer, C. Mitterer, J.G. Wen, J.E. Greene, I. Petrov, Self-organized nanocolumnar structure in superhard TiB₂ thin films, *Appl. Phys. Lett.*, 86 (2005) 131909. <https://doi.org/10.1063/1.1887824>.

[46]. B. Hu, Q. Zhang, L. Niu, J. Liu, J. Rao, X. Zhou, Microsphere assembly of boron-doped Rutile TiO₂ nanotubes with enhanced photoelectric performance. *J Mater Sci: Mater Electron*, 26, (2015) 8915–8921. <https://doi.org/10.1007/s10854-015-3573-3>.

Figure Captions

Fig. 1. SEM micrograph of the as-spun mat (a) and FESEM image of the nanofibrous Ti-Al-O-B powder (TAOB-0.8) (b).

Fig. 2. XPS spectra of the nanofibrous Ti-Al-O-B powder (TAOB-0.8); (a) Ti2p, (b) Al2p, (c) O1s, (d) B2s scans. The black circles mark the raw intensities, the colored lines mark the de-convoluted bonds, and the black line marks the sum of the de-convoluted bonds.

Fig. 3. XRD patterns of nanofibrous Ti-Al-O-B powders with different B/(Ti+Al) molar ratios: (a) TAOB-0.8, (b) TAOB-1.6, and (c) TAOB-2.4.

Fig. 4. FESEM microstructures of nanofibrous Ti-Al-O-B powders with different B/(Ti+Al) molar ratios: (a) TAOB-0.8, (b) TAOB-1.6, and (c) TAOB-2.4.

Fig. 5. EDS spectra of nanofibrous Ti-Al-O-B powders with different B/(Ti+Al) molar ratios: (a) TAOB-0.8, (b) TAOB-1.6, and (c) TAOB-2.4.

Fig. 6. Schematic presentation for the process of nanofibrous Ti-Al-O-B powder formation: (a) a schematic cross-section view of a hybrid polymer/ceramic fiber, including an amorphous Al-O-B and TiO_2 NPs, dissolved in the PVP matrix; (b) the schematic process of solid B_2O_3 formation and cracking by H_2O vapor; (c) the decomposition of $\text{Al}(\text{NO}_3)_3$ and potential formation of Al_2O_3 nuclei; (d) molten B_2O_3 surrounds the Al_2O_3 nuclei, and TiO_2 NPs solids; (e) a ceramic matrix containing solids and liquids remains throughout the fibers; (f) TiO_2 NPs break and boride and borate grain form; (g) the growth of boride and borate grains; (h) the final structure of the T-A-O-B powder; sintered boride, borate, and oxide grains.

Fig. 7. (a) Thermogravimetry (TG) and (b) differential scanning calorimetry (DSC) analysis of the nanofibrous Ti-Al-O-B powders; (c) heat flow variations in the range of 800-1000 °C; and (d) variations of heat derivative to temperature ($d\text{H}/dT$) for TABO-0.8, TAOB-1.6, and TABO-2.4 in the range of 800-1000 °C.

Fig. 8. TEM microstructure of Ti-Al-O-B powders with different B/(Ti+Al) molar ratios: (a) TAOB-0.8, (b) TAOB-1.6, and (c) TAOB-2.4.

Figures

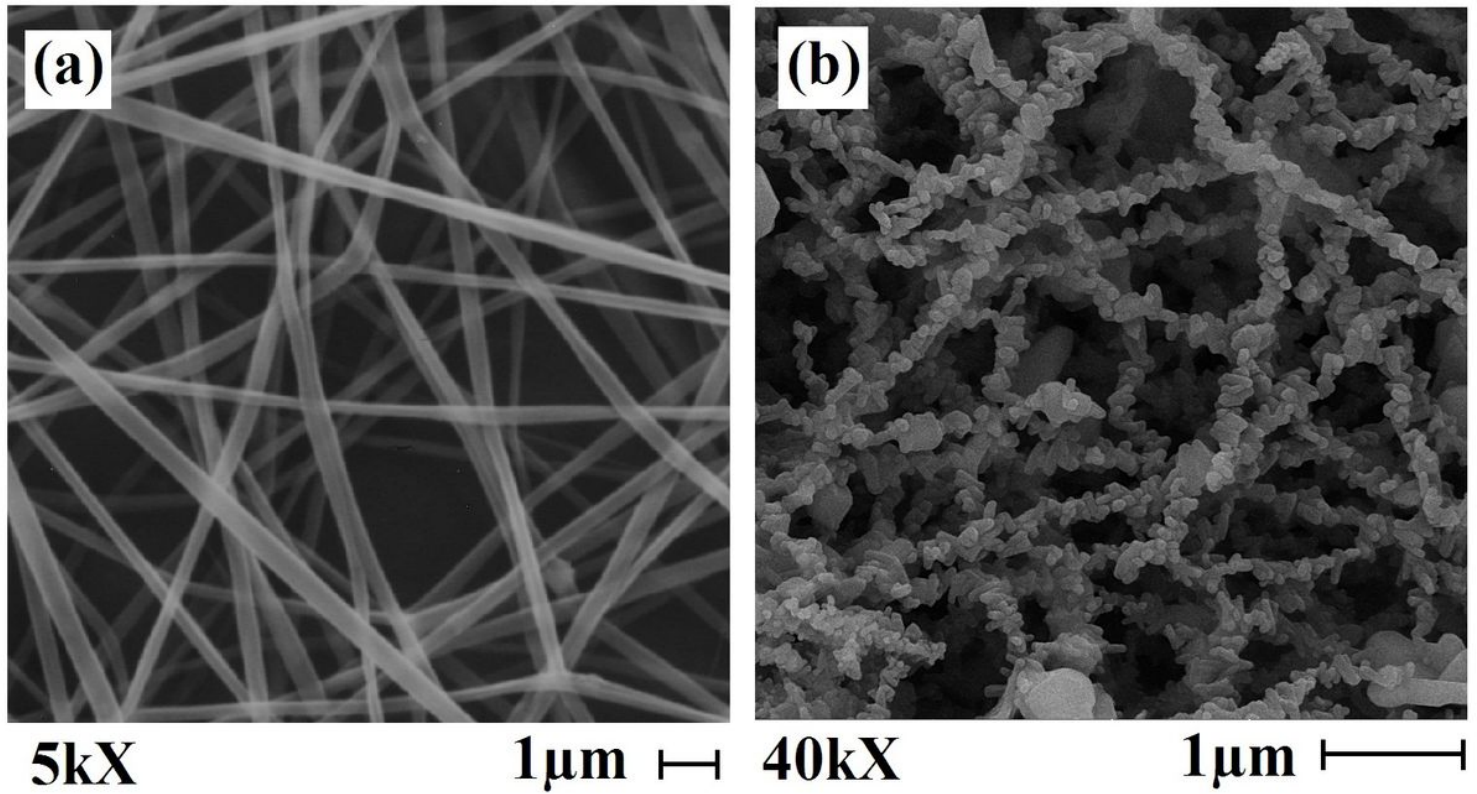


Figure 1

SEM micrograph of the as-spun mat (a) and FESEM image of the nanofibrous Ti-Al-O-B powder (TAOB-0.8) (b).

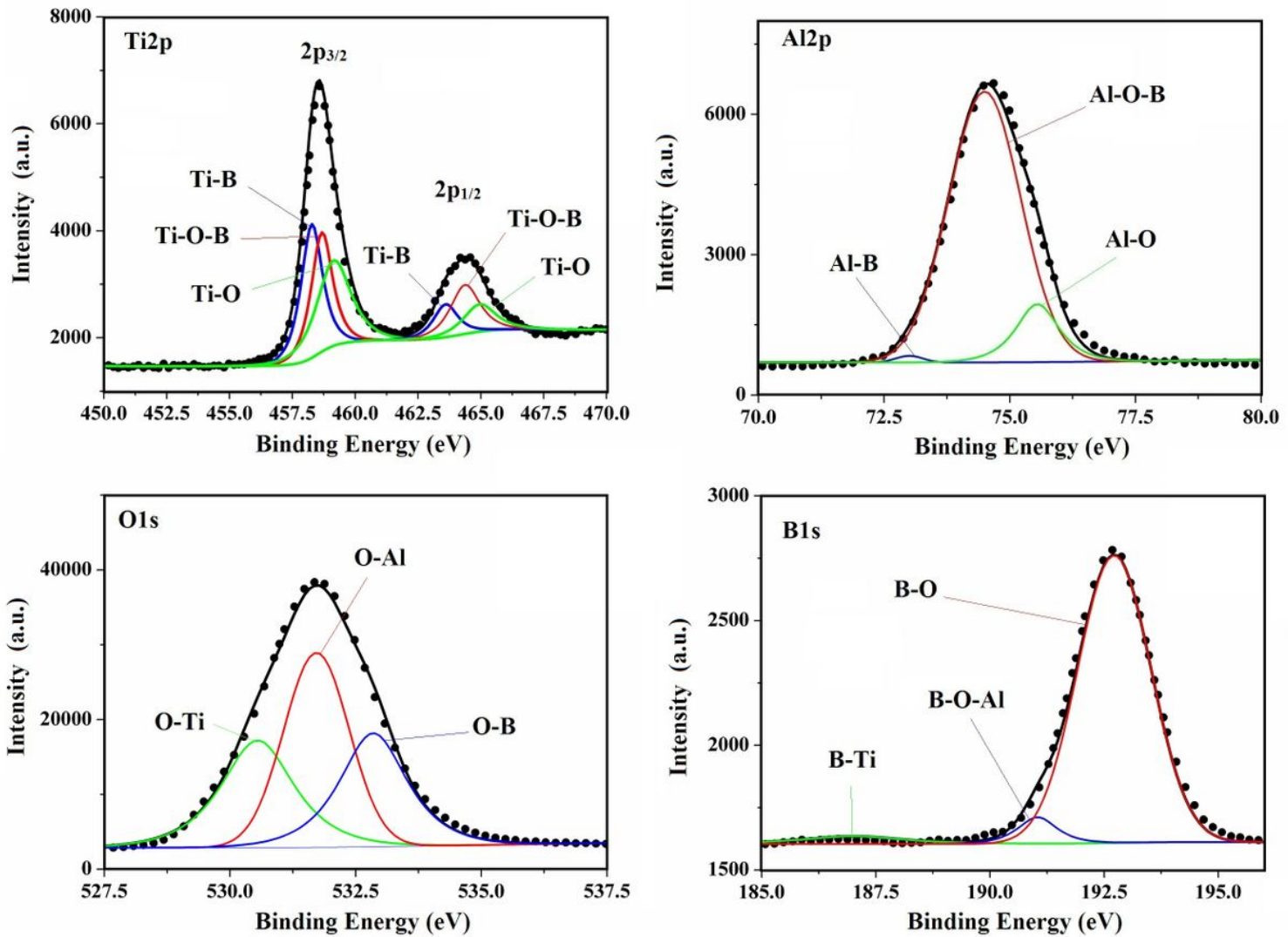


Figure 2

XPS spectra of the nanofibrous Ti-Al-O-B powder (TAOB-0.8); (a) Ti2p, (b) Al2p, (c) O1s, (d) B2s scans. The black circles mark the raw intensities, the colored lines mark the de-convoluted bonds, and the black line marks the sum of the de-convoluted bonds.

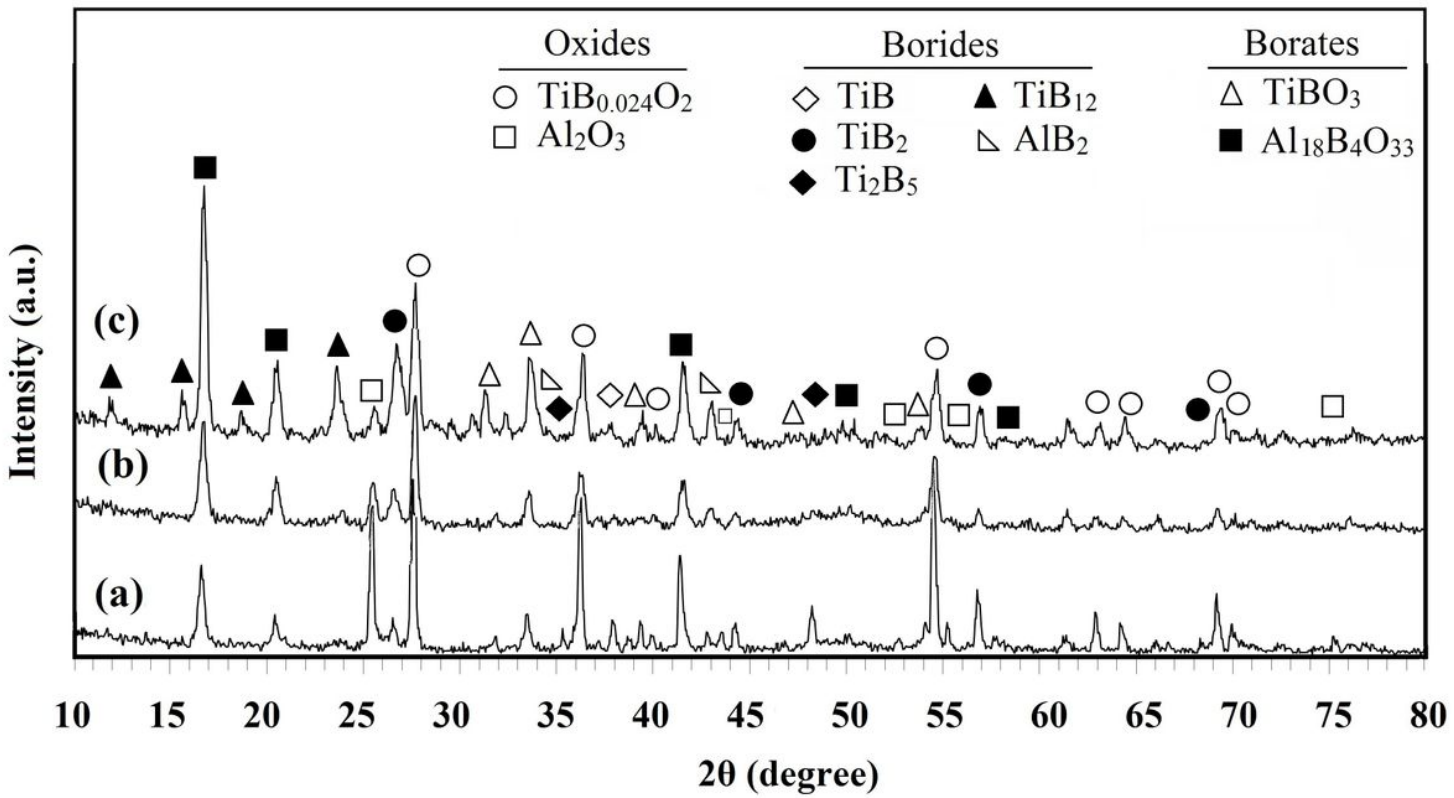


Figure 3

XRD patterns of nanofibrous Ti-Al-O-B powders with different B/(Ti+Al) molar ratios: (a) TAOB-0.8, (b) TAOB-1.6, and (c) TAOB-2.4.

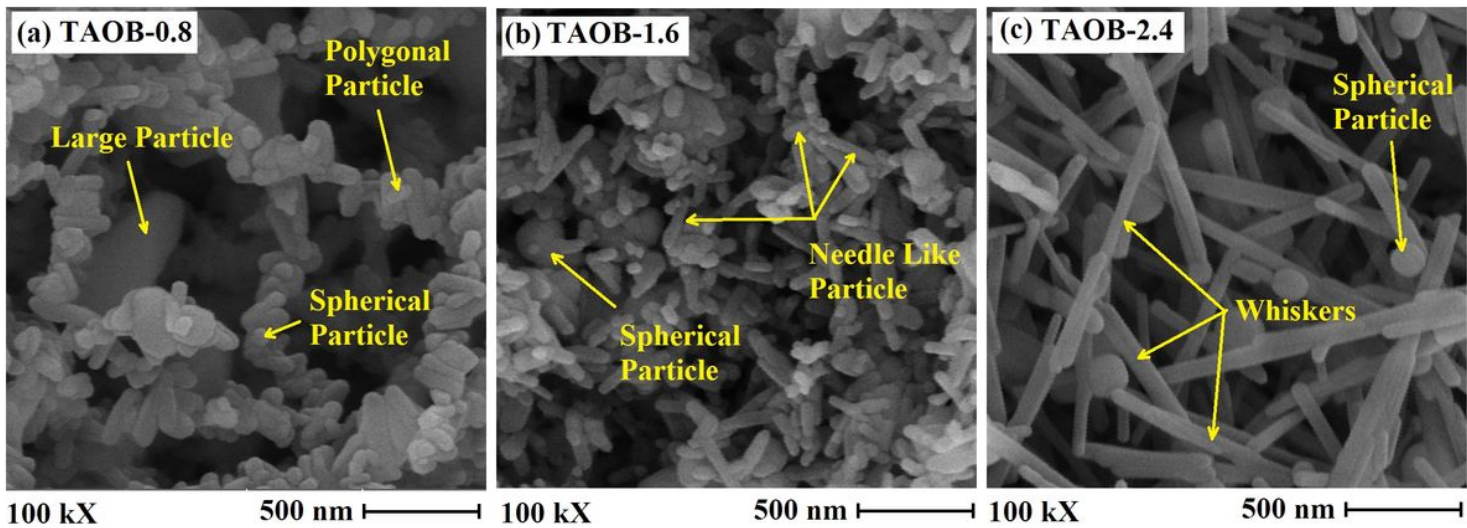


Figure 4

FESEM microstructures of nanofibrous Ti-Al-O-B powders with different B/(Ti+Al) molar ratios: (a) TAOB-0.8, (b) TAOB-1.6, and (c) TAOB-2.4.

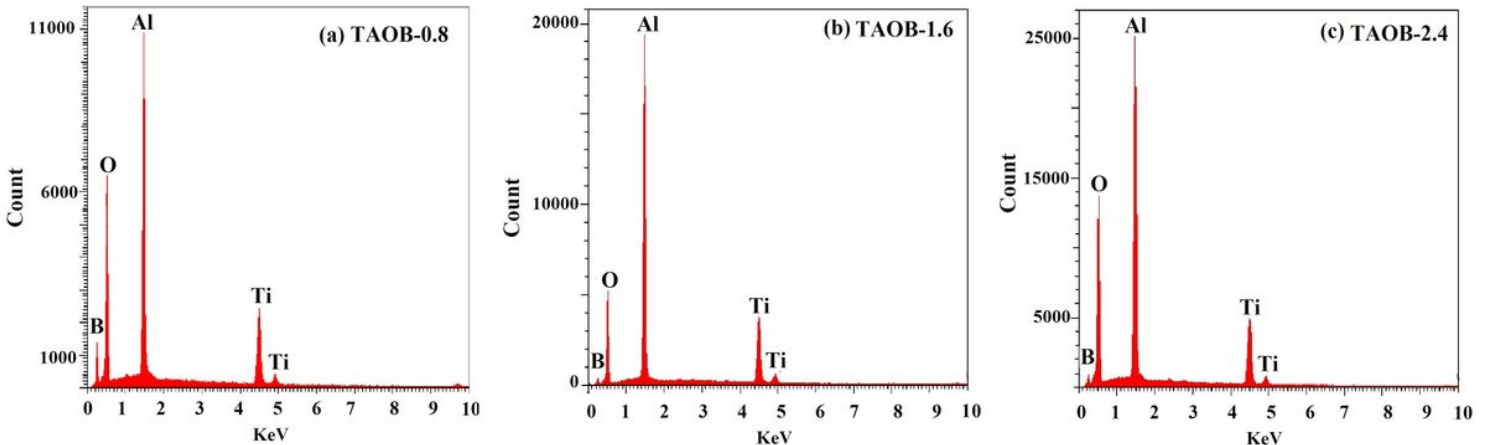


Figure 5

EDS spectra of nanofibrous Ti-Al-O-B powders with different B/(Ti+Al) molar ratios: (a) TAOB-0.8, (b) TAOB-1.6, and (c) TAOB-2.4.

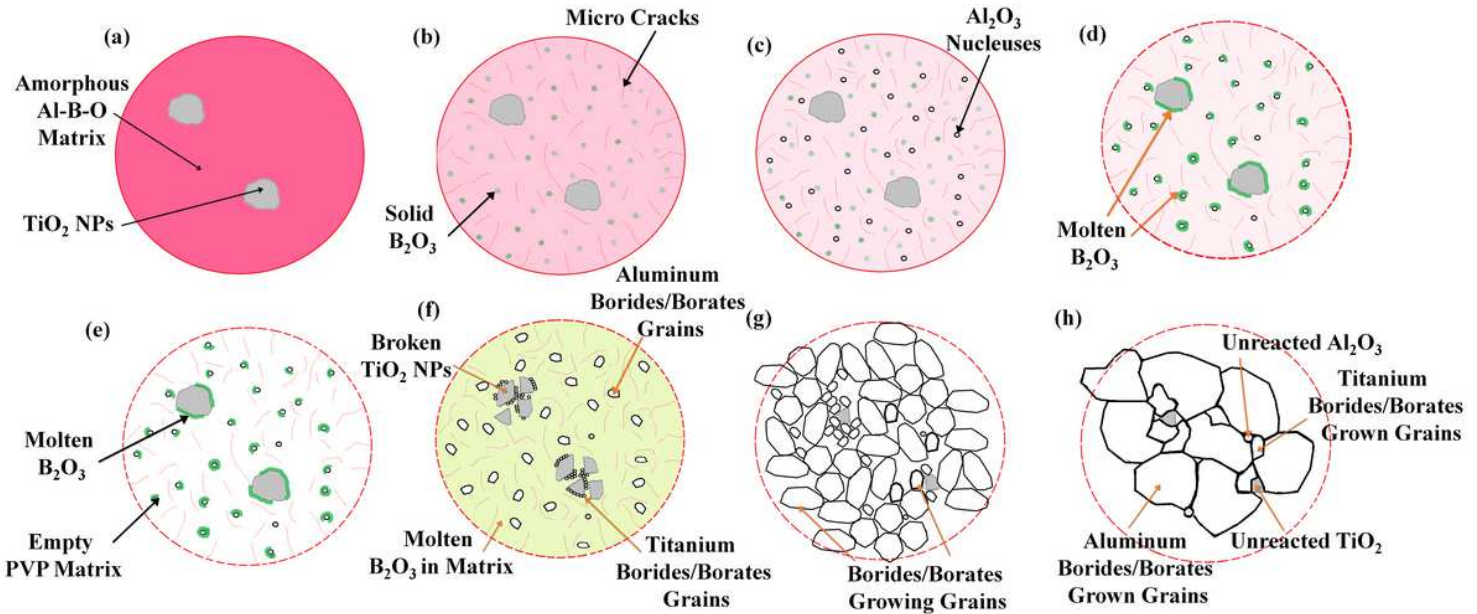


Figure 6

Schematic presentation for the process of nanofibrous Ti-Al-O-B powder formation: (a) a schematic cross-section view of a hybrid polymer/ceramic fiber, including an amorphous Al-O-B and TiO₂ NPs, dissolved in the PVP matrix; (b) the schematic process of solid B₂O₃ formation and cracking by H₂O vapor; (c) the decomposition of Al(NO₃)₃ and potential formation of Al₂O₃ nuclei; (d) molten B₂O₃ surrounds the Al₂O₃ nuclei, and TiO₂ NPs solids; (e) a ceramic matrix containing solids and liquids remains throughout the fibers; (f) TiO₂ NPs break and boride and borate grain form; (g) the growth of boride and borate grains; (h) the final structure of the T-A-O-B powder; sintered boride, borate, and oxide grains.

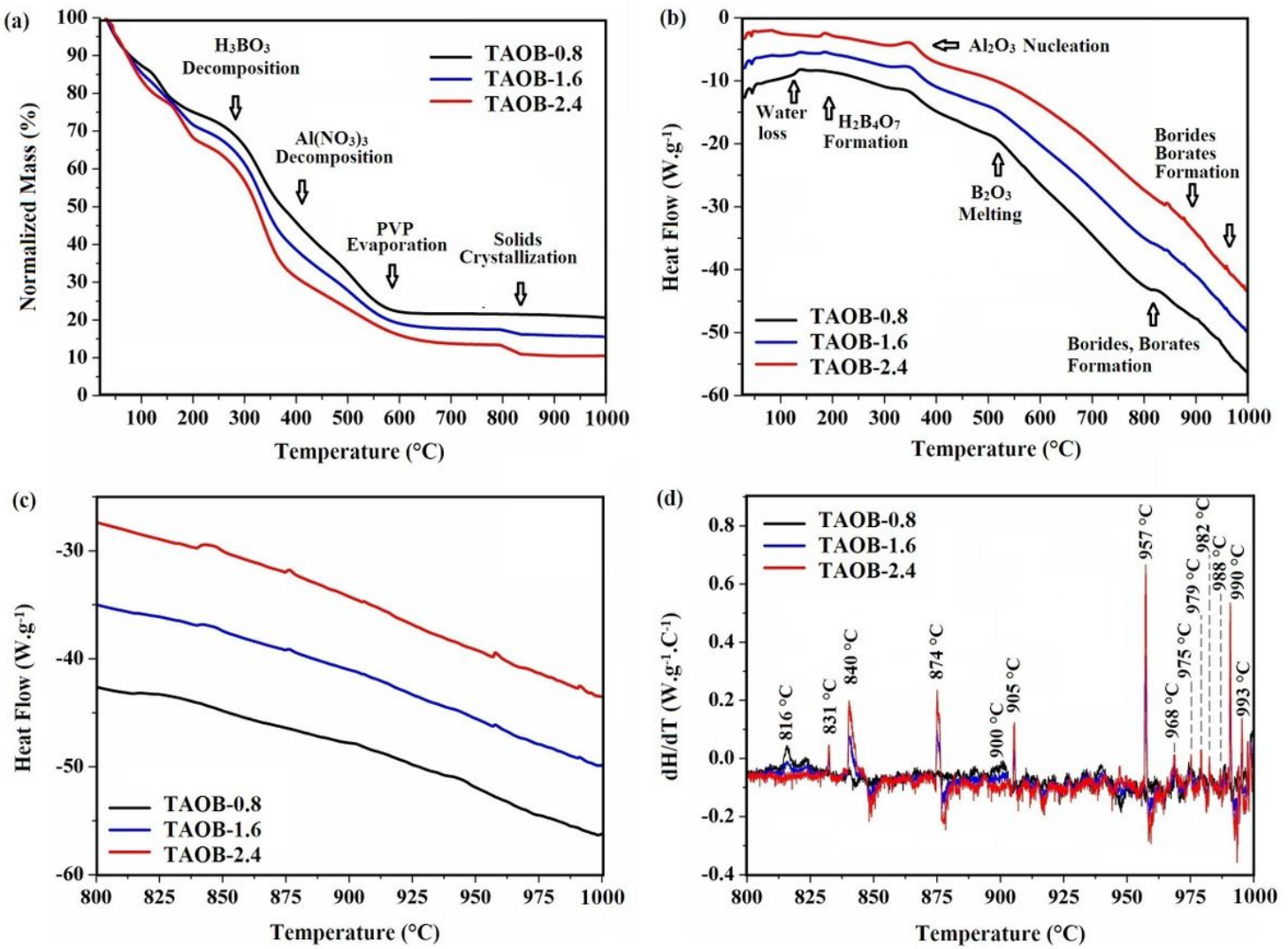


Figure 7

(a) Thermogravimetry (TG) and (b) differential scanning calorimetry (DSC) analysis of the nanofibrous Ti-Al-O-B powders; (c) heat flow variations in the range of 800-1000 °C; and (d) variations of heat derivative to temperature (dH/dT) for TABO-0.8, TAOB-1.6, and TAOB-2.4 in the range of 800-1000 °C.

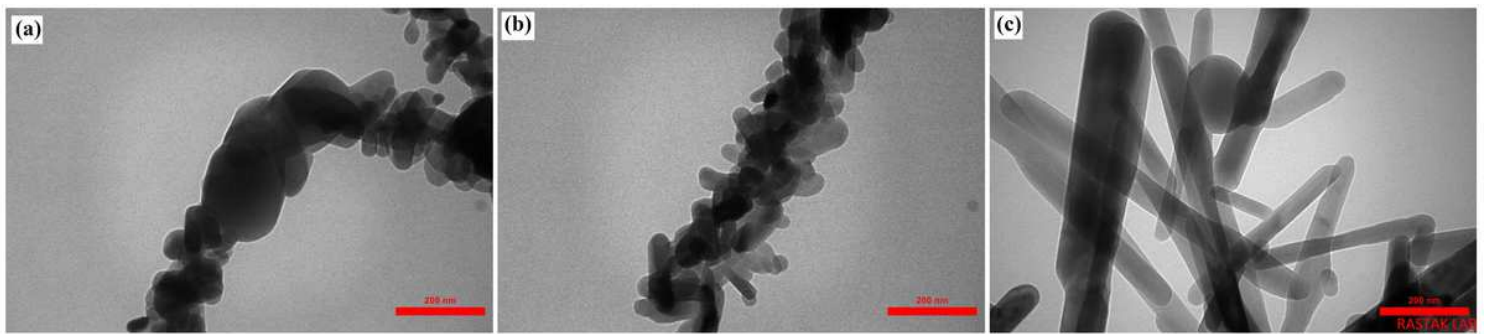


Figure 8

TEM microstructure of Ti-Al-O-B powders with different B/(Ti+Al) molar ratios: (a) TAOB-0.8, (b) TAOB-1.6, and (c) TAOB-2.4.